1-1-2015

3D Fe2(MoO4)3 microspheres with nanosheet constituents as high-capacity anode materials for lithium-ion batteries

Hao Zheng
Hubei University, Anshun University

Shiqiang Wang
Hubei University, Anshun University

Jiazhao Wang
University of Wollongong, jiazhao@uow.edu.au

Jun Wang
University of Wollongong, jw707@uowmail.edu.au

Lin Li
Hubei University, Anshun University

See next page for additional authors

3D Fe2(MoO4)3 microspheres with nanosheet constituents as high-capacity anode materials for lithium-ion batteries

Abstract

Three-dimensional (3D) Fe2(MoO4)3 microspheres with ultrathin nanosheet constituents are first synthesized as anode materials for the lithium-ion battery. It is interesting that the single-crystalline nanosheets allow rapid electron/ion transport on the inside, and the high porosity ensures fast diffusion of liquid electrolyte in energy storage applications. The electrochemical properties of Fe2(MoO4)3 as anode demonstrates that 3D Fe2(MoO4)3 microspheres deliver an initial capacity of 1855 mAh/g at a current density of 100 mA/g. Particularly, when the current density is increased to 800 mA/g, the reversible capacity of Fe2(MoO4)3 anode still arrived at 456 mAh/g over 50 cycles. The large and reversible capacities and stable charge-discharge cycling performance indicate that Fe2(MoO4)3 is a promising anode material for lithium battery applications.

Keywords

3d, batteries, 3, microspheres, nanosheet, constituents, high, capacity, anode, materials, lithium, ion, fe2, moo4

Disciplines

Engineering | Physical Sciences and Mathematics

Publication Details

Zheng, H., Wang, S., Wang, J., Wang, J., Li, L., Yang, Y., Feng, C. & Sun, Z. (2015). 3D Fe2(MoO4)3 microspheres with nanosheet constituents as high-capacity anode materials for lithium-ion batteries. Journal of Nanoparticle Research, 17 (11), 449-1-449-8.

Authors

Hao Zheng, Shiqiang Wang, Jiazhao Wang, Jun Wang, Lin Li, Yun Yang, Chuanqi Feng, and Ziqi Sun

3D $Fe_2(MoO_4)_3$ microspheres with nanosheet constituents as high-capacity anode materials for lithium-ion batteries

Hao Zheng[a,b], Shiqiang Wang[a], Jiazhao Wang[c], Jun Wang[c], Lin Li[a,b], Chuanqi Feng[a]*, Ziqi Sun[c,]*

[a] Key Laboratory for Synthesis and Applications of Organic Functional Molecules, Hubei University, Wuhan 430062, China

[b] Key Laboratory of Functional Materials and Chemistry for Performance and Resources of the Guizhou Education Department, Anshun University, Anshun 561000, China

c Institute for Superconducting and Electronic Materials, University of Wollongong, Innovation Campus, Squires Way, North Wollongong, NSW 2500, Australia

Abstract

Three-dimensional (3D) $Fe_2(MoO_4)_3$ microspheres with ultrathin nanosheet constituents are first synthesized as anode materials for the lithium-ion battery. It is interesting that the single-crystalline nanosheets allow rapid electron/ion transport on the inside, and the high porosity ensures fast diffusion of liquid electrolyte in energy storage applications. The electrochemical properties of $Fe_2(MoO_4)_3$ as anode demonstrates that 3D $Fe_2(MoO_4)_3$ microspheres delivere an initial capacity of 1855 $mAh \cdot g^{-1}$ at a current density of 100 $mA \cdot g^{-1}$. Particularly, when the current density is increased to 800 $mA \cdot g^{-1}$, the reversible capacity of $Fe_2(MoO_4)_3$ anode still arrived at 456 $mAh \cdot g^{-1}$ over 50 cycles. The large and reversible capacities and stable charge-discharge cycling performance indicate that $Fe_2(MoO_4)_3$ is a promising anode material for lithium battery applications.

Keywords: Inorganic compounds; Chemical synthesis; Nanostructures ; Electrochemical properties

Introduction:

Nanostructured materials lie at the centre of fundamental advances for high-efficiency photochemical and electrochemical energy storage/conversion devices.[1-6] In

* Corresponding authors: Tel: +86-27-88662747; E-mail: cfeng@hubu.edu.cn (chuanqi Feng);

Tel: +61-2-4298-1479; Fax: +61-2-4221-5731, Z. Sun, ziqi@uow.edu.au

particular, some nanomaterials in special morphologies (nanobelts, nanotubes, hollow microspheres, core–shell microspheres, mesoporous materials, etc.) are acknowledged as promising solutions for future generations of lithium ion batteries with high energy density, high power density, and excellent cycling stability, because of their large surface areas, short distances for mass and charge transport, and freedom from volume change problems.[7-10]

Metal molybdates have received great attention due to their broad applications in various fields, including sensors and detectors, scintillator materials, and catalysis, as well as their electrochemical and magnetic applications.[11-18] It has been demonstrated that soft chemistry routes (hydrothermal synthesis, self-templated methods, microwave-assisted solution synthesis, etc.) are the best way to controllably synthesize this family of materials.[19-25] Recently, many metal molybdates or tungstates with different morphologies and sizes have been made via the hydrothermal approach to investigate their crystal growth mechanisms or physical properties.[10-25] The lithium storage capabilities of molybdates have also received little attention. For example, Leyzerovich *et al.* introduced $NiMoO_4$ as a cathode material in lithium ion batteries (LIBs) in 2004.[24] It is proposed that its high charge capacity is related to the vacancies in the structure of the $NiMoO_4$ nanorod bundles, in which Li^+ ions could be reversibly incorporated. Ding *et al.* have reported the first discharge capacity of their $NiMoO_4$ nanorods as reaching 850 $mAh \cdot g^{-1}$ for the voltage window between 1.2 and 4.0 V at a current density of 0.1 $mA \cdot cm^{-2}$.[14] The discharge curves have clear voltage plateaus around 1.8 V. The performance is much better than for $CoMoO_4$ (130 $mAh \cdot g^{-1}$) and $MnMoO_4$ (180 $mAh \cdot g^{-1}$). Recently, Haetge *et al.* have reported mesoporous nanocrystalline nickel molybdate ($NiMoO_4$) thin film electrodes.[25] The initial

discharge capacity is 270 $mAh \cdot g^{-1}$ at a rate of 1.4 C within a potential window of 3.5–1.5 V vs. Li/Li^+.

Iron molybdate ($Fe_2(MoO_4)_3$) exhibits very interesting magnetic properties and is a particularly efficient catalyst for the oxidation of methanol to formaldehyde.[19, 26-29] To the best of our knowledge, however, no investigations have been conducted on $Fe_2(MoO_4)_3$ as an anode material for lithium ion batteries so far. In the present work, three-dimensional (3D) $Fe_2(MoO_4)_3$ microspheres with ultrathin, single-crystalline nanosheet architectures were synthesized via a hydrothermal process. It is interesting that the single-crystalline nanosheets allow rapid electron/ion transport on the inside, and the high porosity ensures fast diffusion of liquid electrolyte in energy storage applications. The electrochemical properties of $Fe_2(MoO_4)_3$ have been studied here for the first time as anode material in lithium ion batteries, in order to explore its prospects in future-generation batteries.

Results and discussion

Fig. 1 presents scanning electron microscope (SEM) images of the hierarchical 3D $Fe_2(MoO_4)_3$ microspheres with ultrathin nanosheet constituents synthesized at 180 ^oC. The overall morphology of the samples (Fig. 1(a-b) and Fig. S1) indicates that large-scale microspheres were achieved by using this simple hydrothermal approach. The obtained microspheres have diameters ranging from 5 to 20 μm. As shown in the high-magnification SEM images [Fig. 1(b-c)], the microspheres are composed of numerous ultrathin nanosheets. Fig. 1(d) presents the morphology of the constituent naonsheets from observing the cross-sectional surfaces of the microspheres, in which it is clearly displayed that the nanosheets are around 500 nm in width. The thicknesses of the nanosheets were also estimated from Fig. 1(e). It is interesting that the nanosheets are very thin, around 20-50 nm. From Fig. 1(e), we also find that there is considerable space between the individual nanosheets. This kind of architecture of the constituent nanosheets provides permeation pathways and allows sufficient

diffusion of the reaction solution in further functional applications. The chemical composition of the $Fe_2(MoO_4)_3$ microspheres was analysed by energy dispersive spectroscopy (EDS), as shown in Fig.1(f), indicating that the constituent chemical elements are Fe, Mo, and O in a molar ratio approximately equal to 1: 1.4: 5.8, near to the $Fe_2(MoO_4)_3$ formula. The corresponding X-ray diffraction (XRD) characterization also confirmed the formation of well-crystalized monoclinic $Fe_2(MoO_4)_3$ (Fig. S2 in the Supporting Information).

The microstructure and the crystal structure of the $Fe_2(MoO_4)_3$ nanosheets in the 3D nanosheet microspheres were further characterized by transmission electron microscopy (TEM). Fig. 2(a) shows individual nanosheets after breaking up the $Fe_2(MoO_4)_3$ microspheres by ultrasonication. Fig .2(b) shows the corresponding selected area electron diffraction (SAED) pattern from the nanoplates, which was recorded from the [011] zone axis. Fig. 2(c-d) presents high resolution TEM (HRTEM) images, showing the lattice fringes of the nanosheets, which are in good agreement with the *d*-spacing of the (**Error! Reference source not found.**24) and (212) planes. The white spots verify the single crystalline nature of the $Fe_2(MoO_4)_3$ nanoplates and show that the crystal grows along the [0**Error! Reference source not found.**1] direction.

Fig. 3 shows the first five cyclic voltammetry (CV) curves of the electrode made from the 3D $Fe_2(MoO_4)_3$ microspheres at a scan rate of 0.1 mV/s in the voltage range 0.01~3.0 V vs. Li. The voltammogram for the first cycle is substantially different from those for the subsequent ones. During the first cycle, it showed a broad cathodic peak cantered at 1.33 V, followed by onset of a large voltage peak at 0.3 V and extending up to the 0.049 V, which can be ascribed to the reduction of Fe^{3+} and Mo^{6+} to metallic Fe and Mo, respectively. The main reduction peak shifts to broad peaks at 0.64 and 0.19 V in the subsequent cycles, which might originate from the pulverization of the $Fe_2(MoO_4)_3$. These voltage peaks implied the crystal structure destruction; followed by formation of corresponding metals and amorphous Li_2O (eqn (1)).

During the subsequent oxidation, a broad and intense peak cantered at 1.45 V and a low intensity peak cantered at 1.75 V were observed. The first voltage peak is possibly due to the oxidation of Mo to Mo^{6+} state (i.e. formation of MoO_3) and the later peak is possibly due to the oxidation of Fe to Fe_2O_3,[30] the Mo element was reduced from the higher oxidation state of Mo and hence facilitated the formation of MoO_3 during subsequent oxidation in O-reach environment. These peaks are due to the oxidation of metals to form their corresponding metal oxides (eqn (2) and (3)).

$$Fe_2(MoO_4)_3 + 24Li^+ + 24e^- \longrightarrow 2Fe^0 + 3Mo^0 + 12Li_2O \quad (1)$$

$$2\ Fe + 3Li_2O \leftrightarrow 2\ Fe_2O_3 + 6Li^+ + 4e^- \quad (2)$$

$$3Mo + 9Li_2O \leftrightarrow 3MoO_3 + 18Li^+ + 12e^- \quad (3)$$

The electrochemical performance of the $Fe_2(MoO_4)_3$ was measured via coin cell testing. Fig. 4(a) shows typical discharge/charge cycles of the as-prepared $Fe_2(MoO_4)_3$ electrode cycled between 0.01 and 3.0 V at a current density of 100 $mA \cdot g^{-1}$ at room temperature. The initial discharge capacity of the as-prepared 3D $Fe_2(MoO_4)_3$ microspheres was 1855 $mAh \cdot g^{-1}$. The difference between the first and following cycles could be seen. In the first discharge curves, two voltage plateaus near 1.6 and 0.6 V are clearly observed, and the higher potential peak remains at 0.6 V in the following cycles, while the charge curves of the sample show a de-insertion plateau at about ~1.5 V. Apparently, iron molybdate manifests similar discharge processes with that of nickel molybdite based on the voltage-capacity profiles.[25] The electrochemical intercalation of Li into $Fe_2(MoO_4)_3$ leads to the formation of a two-phase system: Li-Fe-O and Li_2MoO_3, which has not been previously described, with the former phase being redox inactive in the potential window chosen here. It has been reported that the formation of Li-A-O is irreversible and contributes to the irreversible capacity loss in the first cycle in the molybdites.[14, 25] Additionally, the formation of a solid electrolyte interface (SEI)

layer is also partly responsible for the initial irreversible capacity loss. After the first charge/discharge cycle, the electrochemically active Li_xMoO_y conveys reversible electrochemical reactivity toward Li.

Fig. 4(b) shows the cycling performance of the 3D $Fe_2(MoO_4)_3$ microspheres at a current density of 100 $mA \cdot g^{-1}$. The $Fe_2(MoO_4)_3$ microspheres delivered a larger initial capacity of 1855 $mAh \cdot g^{-1}$ (equivalent to ~14.1 mol Li per mole) and show a high reversible capacity of 1382 $mAh \cdot g^{-1}$ for the second cycle, which is much higher than what was reported for metal molybdates.[14, 24-25] It still retains a high capacity of 745 $mAh \cdot g^{-1}$, even after 50 cycles, which is much higher than the theoretical capacity of graphite (372 $mAh \cdot g^{-1}$). What is more, except for the first two cycles, where Coulombic efficiencies are 98%, those of the rest of the cycles are about 100% Coulombic efficient (Fig. 4(b)). It is interesting that there is a deep reduction in the capacity in the first cycle. Based on a previous study on MnO_2, the sloping part is generally considered as due to capacitive behaviour from surface storage of lithium, which has been widely observed in the nanostructured materials with high specific surface areas.[31-32] The improvement in charge storage is likely due to the unique morphology of the material, in particular, the ability to access bulk and surface sites. It is obvious that the $Fe_2(MoO_4)_3$ sample shows much improved cycling performance with higher specific capacity at the same cycle with the same current density as compared with the other samples in the literature.[14,24] The superior battery performance is mainly attributable to the unique micro/nanostructure composed of interconnected $Fe_2(MoO_4)_3$ nanosheets, which provides good electrolyte diffusion and large electrode−electrolyte contact area, while reducing volume change during the charge/discharge process. The strategy is simple but very effective, and because of its versatility, it could be extended to other high-capacity metal oxide anode materials for LIBs.

To better understand the electrochemical behaviour of the 3D $Fe_2(MoO_4)_3$) nanosheet microspheres, we also investigated their rate performance as shown in Fig. 5(a-b). The $Fe_2(MoO_4)_3$ electrode was cycled at various current densities (100−1600 $mAh \cdot g^{-1}$). The cell shows good rate capability with average discharge capacity of 1546, 785, 496, 449, 299, and 212 $mAh \cdot g^{-1}$, when the current density was increased stepwise to 100, 200, 400, 800, 1200, and 1600 $mA \cdot g^{-1}$, respectively. Upon changing the current density back to 100 $mA \cdot g^{-1}$, an average discharge capacity as high as 811 $mAh \cdot g^{-1}$ could be recovered. This demonstrates that the 3D $Fe_2(MoO_4)_3$ nanosheet microspheres have great potential as high-rate anode materials in lithium-ion batteries.

Electrochemical impedance spectrum (EIS) can give information about the solid electrolyte interface, the charge transfer and bulk resistances of the electrodes, and the associated capacitances and variation of the electrodes with the applied voltage during the charge-discharge cycles.[33-34] Fig. 6 presents the impedance plots were obtained for 3D $Fe_2(MoO_4)_3$ electrodes. The presence of a semi-circular loop at higher frequencies is attributed to the faradic reactions. The measured resistance (intercept of semicircle along the *x*-axis) is composed of the ionic resistance of electrolyte, which is the intrinsic resistance of the active material and the contact resistance of the active material/current collector interface. The intermediate frequency region, the 45° tilting tails is the characteristic of Li^+ ion diffusion into the porous structure of the electrode. In the low frequency region, the slop of the impedance plot increases and tends to become purely capacitive, which demonstrate the high electrochemical capacitance of the material. As shown in Fig. 5, the $Fe_2(MoO_4)_3$ electrode exhibited much lower resistance in the higher frequency region at the first 10 cycles, indicating the better electronic conductivity and smaller contact resistance. However, the impedance spectrum of the $Fe_2(MoO_4)_3$ electrode after 50 cycles showed an extremely high charge transfer resistance (Rct = 352 Ω). The increasing charge transfer resistance after

cycling should be aroused by the interconnectivity among the $Fe_2(MoO_4)_3$ 3D microspheres, which undergo a large volume change during the electrochemical conversion reaction. The volume change of the electrodes during the cycling leads to a large mechanical stress and a subsequent structural failure, which then induces an electrical isolation and contact loss within the nanostructured electrodes, and results in an increase in charge transfer resistance.[35] This study revealed that if above problem is solved in our future work, 3D $Fe_2(MoO_4)_3$ microspheres will be the promising anode material with high-capacity for lithium ion batteries. The design of Mo-based anode materials for lithium ion batteries with long cycle life, high reversible capacity, and excellent rate capability, however, have to be further studied, for example, by polymer coating of $Fe_2(MoO_4)_3$ materials and proper fabrication of $Fe_2(MoO_4)_3$/graphene composites.

Conclusions

In summary, 3D $Fe_2(MoO_4)_3$ microspheres with ultrathin nanosheet constituents were successfully synthesized. The 3D $Fe_2(MoO_4)_3$ nanosheet microspheres displayed an initial capacity of 1855 $mAh \cdot g^{-1}$ at a current density of 100 $mA \cdot g^{-1}$. After 50 cycles, the sample still retained a high capacity of 745 $mAh \cdot g^{-1}$. In particular, when the current density was increased to 800 $mA \cdot g^{-1}$, the reversible capacity of $Fe_2(MoO_4)_3$ anode still reached 456 $mA \cdot g^{-1}$ after 50 cycles. These results demonstrate that 3D $Fe_2(MoO_4)_3$ microspheres are promising for application as anode materials in superior future generation lithium-ion batteries due to their enhanced lithium ion storage capabilities.

Appendix A. Supporting information

Supplementary data associated with this article can be found in the online version.

References:

1. G. Yu, X. Xie, L. Pan, Z. Bao, Y. Cui, *Nano Energy*, **3** (2013) 213-234.

2. M. G. Kim, J. Cho, *Adv. Funct. Mater.*, **19** (2009) 1497-1514.

3. P. G. Bruce, B. Scrosati, J. M. Tarascon, *Angew. Chem., Int. Ed.*, **47** (2008) 2930-2946.

4. H. B. Wu, J. Chen, H. Huang, X. W. Lou. *Nanoscale*, **4** (2012) 2526-2542.

5. Z. Q. Sun, J. H. Kim, Y. Zhao, A. Darren, S. X. Dou, *Chem. Commun.*, **49** (2013) 966-968.

6. Z. Q. Sun, T. Liao, Y. Dou, S. M. Hwang, M. S. Park, L. Jiang, J. H. Kim, S. X. Dou, *Nat. Commun.*, **5** (2014) 3813.

7. Y. Wang, G. Z. Cao, *Adv. Mater*., **20** (2008) 2251-2269.

8. Y. G. Guo, J. S. Hu, L. J. Wan, *Adv. Mater*., **20** (2008) 2878-2887.

9. Z. Q. Sun, J. H. Kim, Y. Zhao, F. Bijarbooneh, V. Malgras, Y. Lee, Y. M. Kang, S. X. Dou, *J. Am. Chem. Soc.*, **133** (2011) 19314-19317.

10. L. Ji, Z. Lin, M. Alcotlabi, X. Zhang, *Energy Environ. Sci*., **4** (2011) 2682-2699.

11. Y. Luo, W. Zhang, X. Dai, Y. Yang, S. Fu, *J. Phys. Chem. B*, **113** (2009) 4856-4861.

12. S. Vilminot, G. Andre, M. Kurmoo, *Inorg. Chem*., **48** (2009) 2687-2692.

13. W. Chu, H. Wang, Y. Guo, L. Zhang, Z. Han, Q. Li, S. Fan, *Inorg. Chem*., **48** (2009) 1243-1249.

14. Y. Ding, Y. Wan, Y. L. Min, W. Zhang, S. Yu, *Inorg. Chem*., **47** (2008) 7813-7823.

15. J. A. Rodriguez, S. Chaturvedi, J. C. Hanson, A. Albornoz, J. L. Brito, *J. Phys. Chem. B*, **102** (1998) 1347-1355.

16. S. Yu, B. Liu, M. Mo, J. Huang, X. Liu, Y. Qian, *Adv. Funct. Mater*. **13** (2003) 639-647.

17. X. Cui, S. Yu, L. Li, L. Biao, H. Li, M. Mo, X. Liu, *Chem. Eur. J.*, **10** (2004) 218-223.

18. D. Ma, S. Huang, W. Chen, S. Hu, F. Shi, K. Fan, *J. Phys. Chem. C*., **113** (2009) 4369-4374.

19. J. Cui, W. Wang, L. Zhen, W. Shao, Z. Chen, *CrystEngComm*, **14** (2012) 7025-7030.

20. B. Liu, S. Yu, L. Li, F. Zhang, Q. Zhang, M. Yoshimura, *J. Phys. Chem. B.*, **108** (2004) 2788-2792.

21. Q. Zhang, X. Chen, Y. Zhou, G. Zhang, S. Yu, *J. Phys. Chem. B.*, **111** (2007) 3927-3934.

22. D. Chen, K. Tang, F. Li, H. Zheng, *Cryst. Growth. Des*., **6** (2006) 247-252.

23. Y. Xu, D. Jiang, W. Bu, J. Shi, *Chem. Lett*., **34** (2005) 978-979.

24. N. Leyzerovich, K.G. Bramnik, T. Buhrmester, H. Ehrenberg, H. Fuess, *J. Power Sources*, **127** (2004) 76-84.

25. J. Haetge, I. Djerdj, T. Brezesinski, *Chem. Commun*., **48** (2012) 6726-6728.

26. M. H. Rapposch, J. B. Anderson, E. Kostiner, *Inorg. Chem.*, **19** (1980) 3531-3539.

27. D. Jing, *Catalytic Partial Oxidation of Methane over $Fe_2(MoO_4)_3$ Catalysts*. Master's Thesis, 2010, Chalmers University of Technology, Göteborg, Sweden.

28. G. Jin, W. Weng, Z. Lin, N. F. Dummer, S. H. Taylor, C. J. Kiely, J. K. Bartley, G. J. Hutchings, *J. Catal*., **296** (2012) 55-64.

29. L. Zhang, X. F. Cao, Y. L. Ma, X. T. Chen, Z. L. Xue, *New J. Chem*., **34** (2010) 2027-2033.

30. C. T. Cherian, M. V. Reddy, S. C. Haur and B. V. R. Chowdari, ACS Appl. Mater. Interfaces, 2013, 5, 918–923.

31. X.Q. Yu, Y. He, J. P. Sun, K. Tang, H. Li, L.Q. Chen, X. J. Huang, *Electrochem. Commun*., **11** (2009) 791-794.

32. F. Jiao, P. G. Bruce, *Adv. Mater*., **19** (2007) 657-660.

33. M.V. Reddy, T. Yu, C. Sow, Z.X. Shen, C.T. Lim, G.V. Subba Rao, B.V.R. Chowdari, *Adv. Funct. Mater*., **17** (2007) 2792–2799.

34. B. Das, M.V. Reddy, C. Krishnamoorthi, S. Tripathy, R. Mahendiran, G.V. Subba Rao, B.V.R. Chowdari, *Electrochim. Acta*, **54** (2009) 3360–3373.

35. Y. Liu and X. Zhang, *Electrochim. Acta*, **54** (2009) 4180-4185.

Figure captions:

Figure 1: SEM morphology and chemical composition of $Fe_2(MoO_4)_3$ microspheres composed of ultrathin nanosheets: (a) Low-magnification image, (b) high magnification image of an individual microsphere, (c) enlarged SEM surface view of microsphere, (d) cross-sectional view of the $Fe_2(MoO_4)_3$ microsphere showing the surfaces of the nanosheets, (e) cross-sectional view of the $Fe_2(MoO_4)_3$ microsphere showing the thickness of the nanosheets, and (f) the corresponding EDS spectrum.

Figure 2: (a) Low magnification TEM image of individual $Fe_2(MoO_4)_3$ nanosheets, (b) corresponding SAED pattern, (c) HRTEM image of the nanosheets, and (d) the lattice fringes of the $Fe_2(MoO_4)_3$ nanosheets.

Figure 3: First five cycles of CVs for the 3D $Fe_2(MoO_4)_3$ microspheres electrode at a scan rate of 0.1 mV s−1 in the voltage range of 0.01−3.0 V.

Figure 4: Electrochemical properties of 3D $Fe_2(MoO_4)_3$ microspheres: (a) typical discharge/charge curves for selected cycles, cycled between 0.01 and 3.0 V at 100 $mA \cdot g^{-1}$, (b) cycling performance of discharge capacity at 100 $mA \cdot g^{-1}$.

Figure 5: Rate performance of 3D $Fe_2(MoO_4)_3$ microspheres: (a) discharge/charge curves at various current densities, (b) rate performance of 3D $Fe_2(MoO_4)_3$ electrode.

Figure 6: Nyquist plots of 3D $Fe_2(MoO_4)_3$ microspheres after the first cycle, 10^{th}

cycle and 50th cycle.

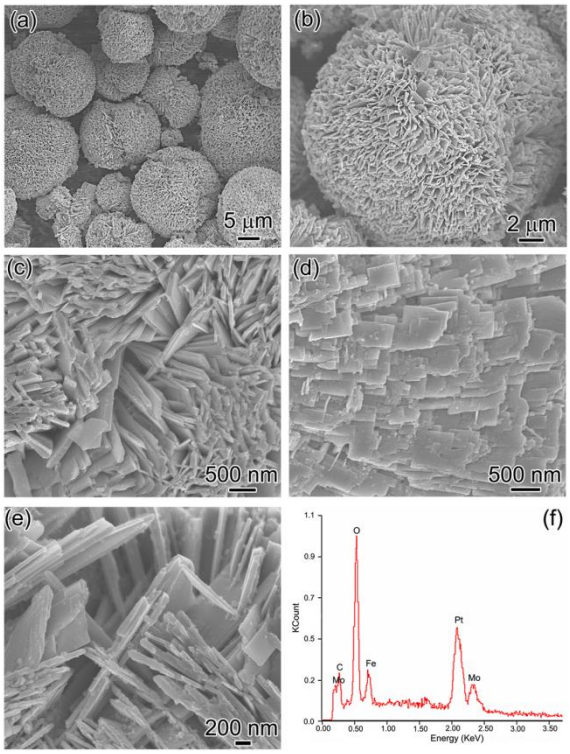

Figure 1

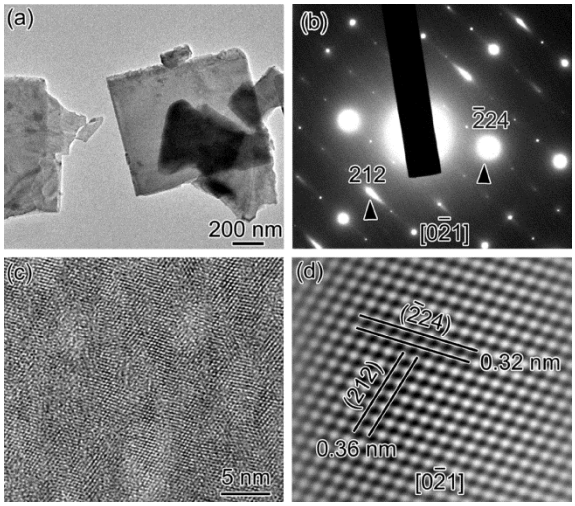
(a)
200 nm
(b)
$\bar{2}24$
212
[$0\bar{2}1$]
(c)
5 nm
(d)
($\bar{2}24$)
0.32 nm
(212)
0.36 nm
[$0\bar{2}1$]

Figure 2

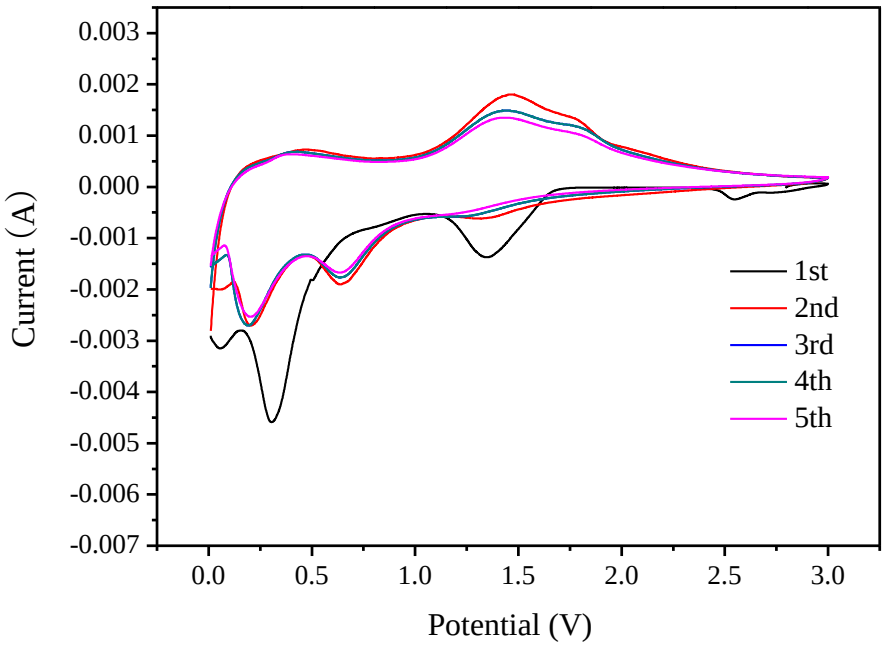
0.003
0.002
0.001
0.000
-0.001
-0.002
-0.003
-0.004
-0.005
-0.006
-0.007
Current (A)
0.0
0.5
1.0
1.5
2.0
2.5
3.0
Potential (V)
1st
2nd
3rd
4th
5th

Figure 3

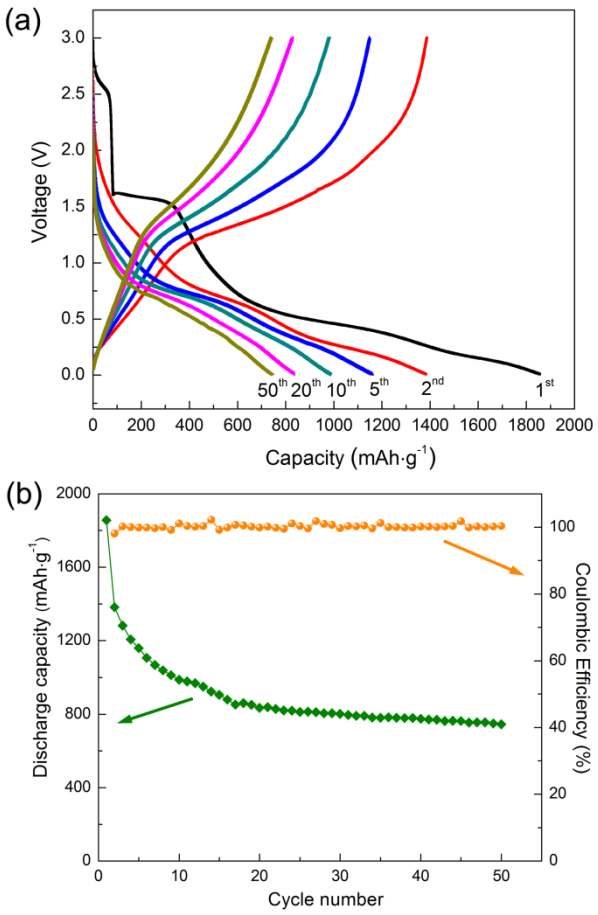
(a)
Voltage (V)
Capacity (mAh·g-1)
50th
20th
10th
5th
2nd
1st
(b)
Discharge capacity (mAh·g-1)
Coulombic Efficiency (%)
Cycle number

Figure 4

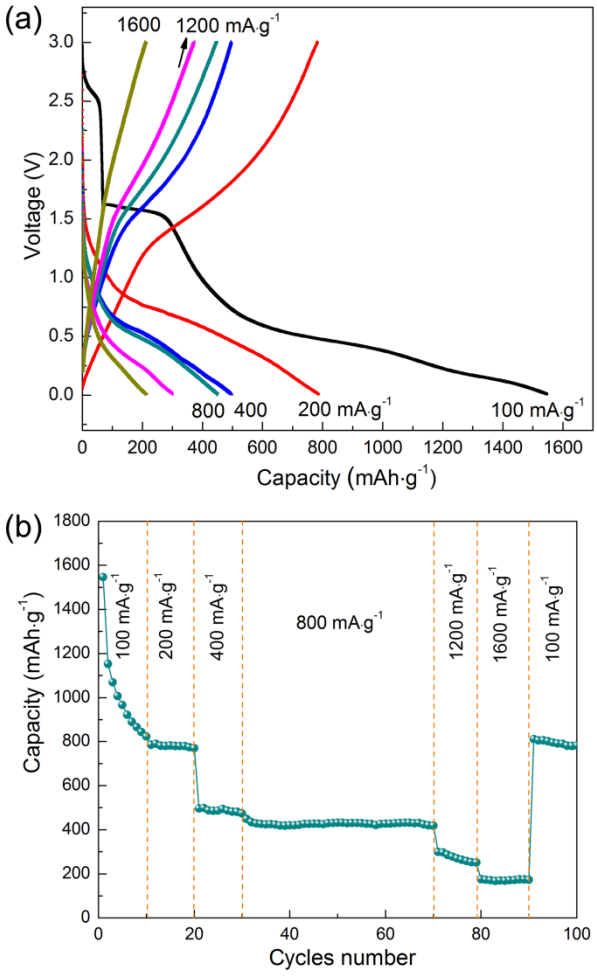
(a)
1600
1200 mA·g-1
800
400
200 mA·g-1
100 mA·g-1
Voltage (V)
Capacity (mAh·g-1)
(b)
100 mA·g-1
200 mA·g-1
400 mA·g-1
800 mA·g-1
1200 mA·g-1
1600 mA·g-1
100 mA·g-1
Capacity (mAh·g-1)
Cycles number

Figure 5

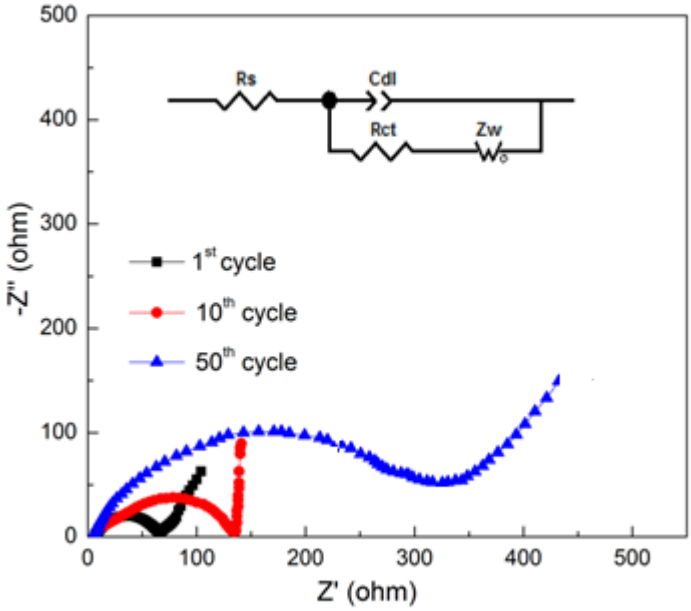
Rs
Cdl
Rct
Zw
1st cycle
10th cycle
50th cycle
-Z'' (ohm)
Z' (ohm)
0
100
200
300
400
500

Figure 6